applied optics

Application of measurement configuration optimization for accurate metrology of sub-wavelength dimensions in multilayer gratings using optical scatterometry

Jinlong Zhu,[1,2,*] Yating Shi,[1] Lynford L. Goddard,[2] and Shiyuan Liu[1]

[1]State Key Laboratory of Digital Manufacturing Equipment and Technology, Huazhong University of Science and Technology, Wuhan 430074, China
[2]Photonic Systems Laboratory, Micro and Nanotechnology Laboratory, Department of Electrical and Computer Engineering, University of Illinois at Urbana-Champaign, Urbana, Illinois 61801, USA
*Corresponding author: jinlongzhu.bryant@gmail.com

Received 25 May 2016; revised 3 August 2016; accepted 4 August 2016; posted 4 August 2016 (Doc. ID 267010); published 23 August 2016

Critical dimension measurement accuracy in optical scatterometry relies not only on the systematic noise level of instruments and the reliability of forward modeling algorithms, but also heavily on the measurement configuration. To construct a set of potentially high-accuracy configurations, we apply a general measurement configuration optimization method based on error propagation theory and singular value decomposition, by which the measurement accuracy is approximated as a function of a pseudo Jacobian with respect to the measurement configurations. Simulations and experiments for the optical metrology of a sub-wavelength deep-etched multilayer grating establish the feasibility of the proposed method.

OCIS codes: (120.0120) Instrumentation, measurement, and metrology; (120.2130) Ellipsometry and polarimetry; (290.3200) Inverse scattering; (050.1950) Diffraction gratings.

http://dx.doi.org/10.1364/AO.55.006844

1. INTRODUCTION

Optical scatterometry, which is rooted in high-precision ellipsometric measurement, is a fast, accurate, non-destructive, and non-contact metrology technique used for measuring the feature dimensions of complex grating structures [1–3]. Nowadays, scatterometry has become a critical technique for in-line wafer-to-wafer process monitoring and control in lithography and etch processes [4–6] because of its inherent advantages over conventional image-based metrology techniques, such as scanning electron microscopy and transmission electron microscopy (TEM).

Scatterometry is a model-based technique where the measured optical signature is fitted by assuming a multi-parameter optical model when calculating the diffraction from a periodic grating to minimize a predefined least-squares (LSQ) function [7–10]. To enable the numerical solution of an LSQ function, abundant measurement information is usually required to make the minimization problem overdetermined, which implies the fact that the measurement signature should be a vector containing multiple data points with variability of measurement conditions such as the wavelength, incident angle, polarization states, and azimuthal angle. The combination of a selected wavelength, an incident angle, a polarization state, and an azimuthal angle is defined as a measurement configuration. Due to the model-driven inherence of optical scatterometry, the output signature sensitivity with respect to the input parameters varies with the measurement configuration [8], which creates the issue of measurement configuration optimization for the selection of the optimal configuration corresponding to the highest measurement accuracy.

Currently, there are some articles aiming at optimizing the measurement configuration for improving either the measurement precision or accuracy. Ku *et al.* proposed a sensitivity analysis-based optimal feature region selection method to seek the signature points containing the most sensitive information about a structure of a surface relief profile for the angle-resolved reflectometry [11]. Vagos and Gross, respectively, proposed an uncertainty analysis scheme and a Jacobian condition number-based method to guide the model and measurement configuration optimization processes [12,13]. Chen *et al.* proposed that by transforming the issue of measurement configuration optimization into a max–min Euclidean norm of the dot product of Jacobians and measurement configurations, the optimal measurement accuracy can be achieved in Mueller matrix-based

scatterometry [14]. Logofatu proposed a sensitivity analysis for a fitting method by defining the sensitivity as the estimated precision of the structural parameters to optimize the measurement configuration for angle-resolved rotating analyzer and angle-resolved phase-modulation scatterometers [15,16]. The above methods demonstrate their success in a specific type of optical scatterometry. Recently, we proposed a general measurement configuration optimization method that is suitable for all types of optical scatterometry [17]. The foundation of this method includes the theoretical analysis of the error propagation similar to the sensitivity analysis program [18–20] and singular value decomposition, by which we show that the measurement configuration optimization can be formulated as a max–min problem of an objective function with respect to the Frobenius norm of the pseudo Jacobian. Instead of using an optimization algorithm such as the gradient-based method to minimize the objective function [14] for picking out only the so-called "optimized" measurement configuration, our method seeks a set of measurement configurations that has the potential to include the optimal one because the objective function is derived by a series of approximations and includes assumptions about the measurement errors, and so its minimization may not necessarily lead to the truly optimal configuration. In our prior work [17], we validated the method using a single-layer etched silicon grating with a period of 800 nm. The grating was optically resolved, since its period is much larger than the illumination wavelength. In this paper, we further validate the proposed method by demonstrating that it can be used to find configurations that can accurately reconstruct sub-wavelength features contained in a much more complicated multilayer structure consisting of silicon, silicon dioxide, and silicon nitride.

We should also mention that the proposed method is not only useful in optical scatterometry, but would also be applicable in the closely related field of optical wafer defect detection. Two of its primary implementation methods, namely, interferometric [21–23] and through-focus microscopy [24–26], also rely on generating overdetermined measurement data using multiple measurement configurations.

We organize the rest of the paper as follows. We introduce the inverse problem in optical scatterometry and the definition of the measurement configuration optimization procedure in Section 2. The detailed derivation can be found in Ref. [17]. In Section 3, we discuss the experimental setup consisting of a measurement instrument as well as the profile details of the investigated sample. Next, in Section 4, we show the simulation and experimental results to establish the validity of the optimization method. Finally, conclusions are drawn in Section 5.

2. METHODOLOGY

Without losing generality, the inverse problem in optical scatterometry is formulated as an object to minimize an LSQ function, which can be expressed as [27]

$$\hat{\mathbf{x}} = \arg\min_{\mathbf{x}\in\Omega}\{[\mathbf{y} - \mathbf{f}(\mathbf{x}, \mathbf{a}^*)]^{\mathrm{T}}\mathbf{w}[\mathbf{y} - \mathbf{f}(\mathbf{x}, \mathbf{a}^*)]\}, \tag{1}$$

where $\mathbf{y}$ is the measured signature as a vector containing m data points. $\mathbf{f}(\mathbf{x}, \mathbf{a}^*)$ is the calculated signature that depends on the profile parameters under measurement $\mathbf{x}$ as an n-dimensional vector $\mathbf{x} = [x_1, x_2, \ldots, x_n]^{\mathrm{T}}$ and the given optimal measurement configuration $\mathbf{a}^*$, which, in general consists of a set of m combinations of wavelength λ, incident angle θ, and azimuthal angle φ. $\mathbf{w}$ is an $m \times m$ diagonal matrix with diagonal elements $\{w_j\}$ representing the jth weight factor. $\hat{\mathbf{x}}$ is the solution of the inverse problem and Ω is the associated parameter domain. Assuming a structural parameter vector $\mathbf{x}$ is close enough to the true parameter vector $\mathbf{x}^*$ under a measurement configuration $\mathbf{a}$, and the function $\mathbf{f}(\mathbf{x}, \mathbf{a})$ is sufficiently smooth, then the function value $\mathbf{f}(\mathbf{x}^*, \mathbf{a})$ can be expanded in the vicinity of $\mathbf{x}$ using the first-order Taylor expansion formulation

$$\begin{aligned}\mathbf{f}(\mathbf{x}^*, \mathbf{a}) &= \mathbf{f}(\mathbf{x}, \mathbf{a}) + \mathbf{J}(\mathbf{x}, \mathbf{a}) \cdot (\mathbf{x}^* - \mathbf{x}) \\ &= \mathbf{f}(\mathbf{x}, \mathbf{a}) - \mathbf{J}(\mathbf{x}, \mathbf{a}) \cdot \Delta\mathbf{x},\end{aligned} \tag{2}$$

where $\mathbf{J}(\mathbf{x}, \mathbf{a})$ is the Jacobian with respect to $\mathbf{x}$ and $\mathbf{a}$, and $\Delta\mathbf{x}$ represents the error in $\mathbf{x}$ and is given by $\Delta\mathbf{x} = \mathbf{x} - \mathbf{x}^*$. For simplicity, we will use $\mathbf{J}$ to take the place of $\mathbf{J}(\mathbf{x}, \mathbf{a})$ in the following content. Note that in Eq. (2), $\Delta\mathbf{x}$ is a function of $\mathbf{J}$ and has no relationship with the measured signature $\mathbf{y}$; thus, it is natural to consider optimizing $\mathbf{J}$ for minimizing $\Delta\mathbf{x}$. We define the optimal set $\mathbf{A}$ of measurement configurations as

$$\mathbf{A} = \{\mathbf{a} | \max_{\mathbf{x}\in\Xi}(\|\tilde{\mathbf{J}}\|_F) < \delta, \delta \in R^+, \mathbf{a} \in \Theta\}, \tag{3}$$

where Θ is the domain of measurement configuration $\mathbf{a}$ and $\tilde{\mathbf{J}}$ is the pseudo Jacobian given by $\tilde{\mathbf{J}} = (\mathbf{J}^{\mathrm{T}}\mathbf{w}\mathbf{J})^{-1}\mathbf{J}^{\mathrm{T}}\mathbf{w}$. $\|\cdot\|_F$ represents the Frobenius norm, which is the matrix norm or vector norm of a matrix or a vector defined as the square root of the sum of the absolute squares of its elements. The detailed derivation of Eq. (3) is given in Ref. [17]. Equation (3) needs some interpretations. The term $\max_{\mathbf{x}\in\Xi}(\|\tilde{\mathbf{J}}\|_F)$ indicates that we first search for the maximal $\|\tilde{\mathbf{J}}\|_F$ in a small vicinity Ξ of the nominal parameter vector $\mathbf{x}$ under a given measurement configuration $\mathbf{a}$. At each measurement configuration, we have a specific maximal $\|\tilde{\mathbf{J}}\|_F$, then by scanning the domain Θ and picking out those measurement configurations $\mathbf{a}$ that lead to the term $\max_{\mathbf{x}\in\Xi}(\|\tilde{\mathbf{J}}\|_F)$ smaller than a pre-selected positive real number δ, the optimal set $\mathbf{A}$ of measurement configuration can be obtained. Each element in $\mathbf{A}$ is a potential measurement configuration that corresponds to the relatively small $\sum_{k=1}^{n}|\Delta x_k|$. The number of elements in $\mathbf{A}$ is a function of δ, the choice of which depends on the user's belief about the reliability of the measurement configuration optimization procedure.

3. EXPERIMENT SETUP AND SAMPLE DESCRIPTION

A dual-rotating-compensator (DRC) Mueller matrix ellipsometer (MME) (RC2 ellipsometer, J. A. Woollam Co.) suitable for a spectrum from ultraviolet to infrared, as presented in Fig. 1, and a self-developed optical modeling software based on the rigorous coupled-wave analysis (RCWA) [28–30] is used for demonstration. As labeled in Fig. 1, the DRC-MME considered in the present paper allows the variation of incident angle θ and azimuthal angle φ, while the wavelength λ is automatically scanned in the range of 200–800 nm and the sample position is fixed. In this paper, the monochromator resolution is set as 10 nm both in the simulation and experiment, which implies the number of measurements m is set as 61. Hence,

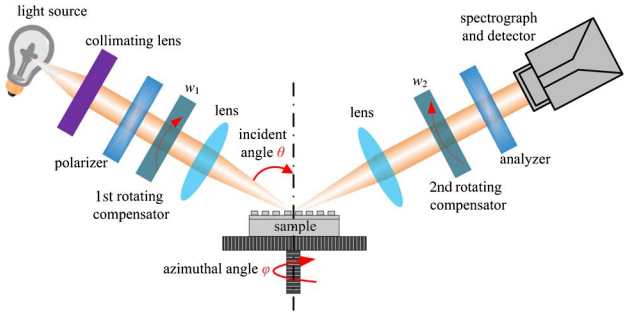

Fig. 1. Measurement setup of the DRC-MME. The ellipsometer primarily consists of the light source, the polarizer, the first rotating compensator, the sample, the second rotating compensator, the analyzer, the spectrograph, and detector. The first and second compensators rotate synchronously at $w_1 = 5w$ and $w_2 = 3w$, where w is the fundamental mechanical frequency.

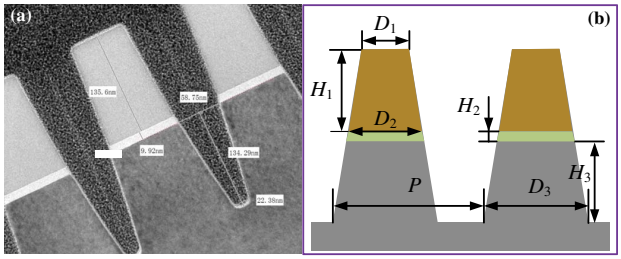

Fig. 2. (a) Cross-section image (reprinted with permission [29]) and (b) geometrical model of the deep-etched multilayer grating consisting of Si, SiO_2, and Si_3N_4 trapezoidal gratings from bottom to top.

in this paper, the measurement configuration should be defined as $\mathbf{a} = [\theta, \varphi]$ because m wavelengths used is fixed.

A deep-etched multilayer grating with whose cross-section image is measured by TEM (TE20, TEM.FEI Co.) is reported here. As presented in Fig. 2(a), this sample consists of Si, SiO_2, and Si_3N_4 trapezoidal gratings from bottom to top [31]. Here, the geometrical model of the deep-etched multilayer grating, as shown in Fig. 2(b), consists of the top critical dimensions (CD) D_1 and D_2 of the Si_3N_4 layer and SiO_2 layer, respectively, the bottom CD of the Si layer, and the thicknesses H_1, H_2, and H_3 of the Si_3N_4 layer, the SiO_2 layer, and the Si layer, respectively. The TEM measured values of the above parameters are $D_1 = 75.01$ nm, $H_1 = 135.60$ nm, $D_2 = 86.90$ nm, $H_2 = 9.92$ nm, $D_3 = 124.13$ nm, $H_3 = 134.29$ nm, and pitch $P = 154$ nm. In the following, we will fix the pitch and allow the remaining geometrical parameters to float.

4. RESULTS

In this section, we first perform the simulation for the deep-etched multilayer grating as presented in Fig. 2(b). We calculate the corresponding Mueller matrix of a "perfect" deep-etched multilayer grating with the profile parameters D_1, H_1, D_2, H_2, D_3, and H_3, respectively, set as the values [75, 135, 90, 10, 130, 132] nm, after which different types of errors will be added into the calculated pure signature. As described in Ref. [17], the errors include the random errors $\boldsymbol{\varepsilon}$, the additive system errors $\boldsymbol{\mu}$, and the non-additive system error contained in the actual forward modeling operator. We first simulate the above three types of errors by considering several main error sources. The random errors $\boldsymbol{\varepsilon}$ and the additive system errors $\boldsymbol{\mu}$ mainly arise from the fluctuation of the measured light fluxes [27] and the bias in a system-independent vector, respectively; the standard deviations of $\boldsymbol{\varepsilon}$ and the specific elements of $\boldsymbol{\mu}$ can both be set as a fraction of the root mean square (rms) in the Mueller matrix over the full wavelength range of interest [7]. The fractions of the wavelengths differ from each other but are all set within the range of 0%–5% in this paper. Each diagonal element of $\mathbf{w}$ presented in Eq. (1) is set as the absolute square of the reciprocal of the standard deviation of a random error corresponding to a specific wavelength channel, which implies that Eq. (1) is equivalent to the maximum-likelihood function, as presented in Ref. [27]. The simulation of the non-additive system error contained in $\mathbf{F}(\mathbf{x}^*, \mathbf{a})$ is more complicated than that of $\boldsymbol{\varepsilon}$ and $\boldsymbol{\mu}$, which in the present paper is simulated by considering the finite numerical aperture of the RC2 ellipsometer, the mechanical positioning errors σ_θ and σ_φ of θ and φ, respectively, and the spectral resolution of the monochromator. The values of σ_θ and σ_φ are set as 0.5° and 1.0° for all the measurement configurations, respectively. The monochromator resolution is set to $\sigma_\lambda = 10$ nm. At a specific measurement configuration $\mathbf{a} = [\theta, \varphi]$, we can calculate the corresponding contaminated Mueller matrix by following the above simulation process, after which we find the maximal $\|\tilde{\mathbf{J}}\|_F$ in the vicinity of the nominal values of D_1, H_1, D_2, H_2, D_3, and H_3. Here, we define the vicinity as the ranges of 65–85 nm, 125–145 nm, 80–100 nm, 5–15 nm, 120–140 nm, and 122–142 nm for D_1, H_1, D_2, H_2, D_3, and H_3, respectively. By picking out the set of $\|\tilde{\mathbf{J}}\|_F$ that is smaller than a preselected δ from all the maxima, the optimal measurement configuration is expected to be among the set of measurement configurations. The ranges of θ and φ considered in this paper are 45°–65° and 0°–90°, respectively, and the increments of each are, respectively, set as 5° and 15°. We present the Frobenius norm of the error propagation matrix $\|\tilde{\mathbf{J}}\|_F$ and the corresponding sum of absolute values of the geometrical parameter departures in Figs. 3(a) and 3(b), respectively. As can be observed, the term $\sum_{k=1}^{n} |\Delta x_k|$ reaches the largest values at a 60° azimuthal angle. This may arise from the fact that the sensitivity of some geometrical parameters with respect to the signature is small under this configuration; thus, the artificially

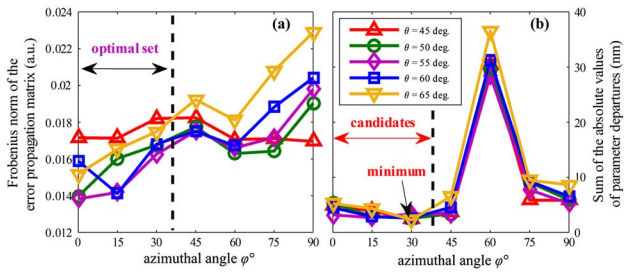

Fig. 3. (a) Frobenius norm of the error propagation matrix and (b) sum of the absolute values of geometrical parameter departures versus the azimuthal angle for several choices of incident angle.

introduced "measurement" errors strongly affect the parameter extraction and lead to large uncertainties for those parameters with small sensitivity. We then set δ as 0.019 and pick out those configurations that are located to the left of the dashed line in Fig. 3(a) to form the set **A**. As expected, the values of the term $\sum_{k=1}^{n}|\Delta x_k|$ corresponding to the configurations in set **A** are all very small when compared with that of the rest of the configurations. We should also note that the minimum of $\sum_{k=1}^{n}|\Delta x_k|$ is also included in the candidates with respect to set **A**. To further present the advantage of the proposed method, we pick out the Frobenius norm and the absolute sum of parameter departures that correspond to $\varphi = 30°$ and list them in Table 1. These values are all within the range of the optimal set, as can be seen in Fig. 3(b). From Table 1, we can find that for different incident angles, the extracted absolute sums of parameter departures are all quite small, and the smallest one is even smaller than 4 nm, which directly demonstrates the feasibility of the proposed method. On the basis of the simulation results, we further perform the experiment for demonstrating the effectiveness of the proposed method.

The Mueller matrices (normalized to m_{11}) corresponding to the deep-etched multilayer grating were measured at 61 points over wavelengths ranging from 200 to 800 nm with the resolution set as 10 nm, the incidence angle was fixed at 60°, and the azimuthal angle varying in the range of 2°–87°, with the resolution set as 5°. The standard deviations of random errors $\boldsymbol{\varepsilon}$ of our DRC-MME are pre-estimated by a signal-dependent noise model introduced by the optical imaging systems [32,33], which implies that the matrix **w** presented in Eq. (1) is a constant matrix throughout the experiment. Note that it is not possible to know the actual geometrical values; thus, we make a trade-off here to just treat the TEM measured ones, which are $D_1 = 75.01$, $H_1 = 135.60$, $D_2 = 86.90$, $H_2 = 9.92$, $D_3 = 124.13$, and $H_3 = 134.29$ nm, as the actual values. This trade-off is reasonable since TEM has been demonstrated as one of the most accurate tools in CD metrology of the semiconductor industry [34]. The procedure as presented in Section 2 and in Ref. [17] is performed to calculate the experimental Frobenius norm of the error propagation matrix, whose results are presented in Fig. 4.

Table 1. Frobenius Norm and the Absolute Sum of Parameter Departures Corresponding to $\varphi = 30°$ (the Units of the Parameters "F-norm" and "Sum" are, Respectively, [1/nm] and [nm])

	$\theta = 45°$	$\theta = 50°$	$\theta = 55°$	$\theta = 60°$	$\theta = 65°$
F-norm	0.0182	0.0168	0.0163	0.0168	0.0175
Sum	3.99	4.28	4.32	5.04	4.23

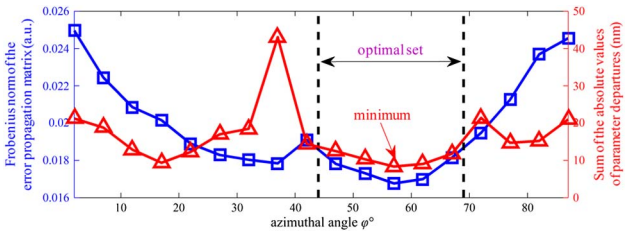

Fig. 4. Optimal set of $\|\tilde{\mathbf{J}}\|_F$ and the corresponding sums of the absolute values of parameter departures for the deep-etched multilayer grating.

As can be seen from the left part of Fig. 4, the Frobenius norm $\|\tilde{\mathbf{J}}\|_F$ has different values under different azimuthal angles, and its minimum can be obtained at the angle of 57°. We believe that the minimal summation of the absolute values of the parameter departures $\sum_{k=1}^{n}|\Delta x_k|$ can be obtained in the vicinity of 57°. Therefore, we set δ as 0.019 and picked out 47°, 52°, 57°, 62°, and 67° as the candidates to form the optimal set **A**. Obviously, as can be seen from the right part of Fig. 4, the minimum that corresponds to the angle 57° is included in the optimal set **A**. We then pick out the Frobenius norm and the absolute sum of parameter departures that correspond to the optimal set and list them in the left section of Table 2. Additionally, we also picked out the Frobenius norm and the absolute sum of parameter departures corresponding to the "marginal" azimuthal angles of the optimal set, which are 42° and 72°, and listed them in the last two columns of Table 2. Obviously, the "marginal" azimuthal angles present not only the larger Frobenius norm, but also the larger absolute sums of parameter departures than those of the elements in the optimal set. We then present the absolute values of parameter departures corresponding to different geometrical parameters in Fig. 5. Interestingly, the absolute values of parameter departures corresponding to the height parameters in the optimal set nearly are all smaller than that out of the optimal set, while this trend is not observed for the CDs, as can be seen from the "marginal" parts of Fig. 5. This means that the proposed method seems to make a trade-off between the CDs and height parameters so that overall, the optimal set choices have relatively small sum of parameter departures. The above results have demonstrated that the proposed method is helpful in achieving relatively high accuracy in optical scatterometry. But, one should keep in mind that this method is an approximate method, which means that if the term $\sum_{k=1}^{n}\sqrt{\sum_{i=1}^{r}\tilde{g}_{ik}^2}$ dominates the overall residuals in the LSQ fitting, then the curve of $\|\tilde{\mathbf{J}}\|_F$ will differ from that of $\sum_{k=1}^{n}|\Delta x_k|$, as can be seen from the left part of the first dashed

Table 2. Frobenius Norm and the Absolute Sum of Parameter Departures Corresponding to the Elements in the Optimal Set (the Units of the Parameters "F-norm" and "Sum" are, Respectively, [1/nm] and [nm])[a]

	$\varphi = 47°$	$\varphi = 52°$	$\varphi = 57°$	$\varphi = 62°$	$\varphi = 67°$	$\varphi = 42°$	$\varphi = 72°$
F-norm	0.0178	0.0173	0.0168	0.0170	0.0182	0.0191	0.0195
Sum	12.47	10.33	8.37	9.06	11.80	14.40	21.38

[a]Note that $\theta = 60°$.

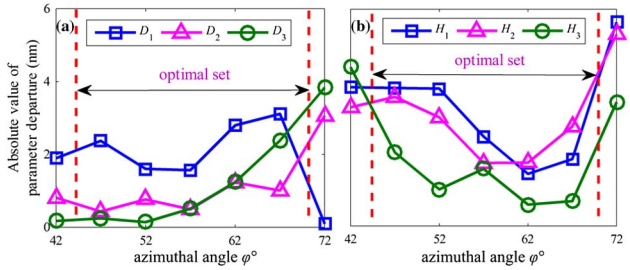

Fig. 5. Absolute values of parameter departures corresponding to (a) CDs D_1, D_2, and D_3, and (b) height parameters H_1, H_2, and H_3, respectively. The points in the light red square represent the ones in the optimal set.

line in Fig. 4. We also note that the optimal set in the Fig. 3(a) simulation is different from that in the Fig. 4 experiment. This may arise from the model imperfection of the multilayer grating, such as the lack of the modeling of round corners at the bottom and roughness [35,36].

We should emphasize that when using the proposed method for measurement configuration optimization, care should be taken in selecting the geometrical parameters and their units because the use of geometrical parameters with different units (for example, nm for CD and degree for sidewall angle) may result in ambiguous terms for $\sum_{k=1}^{n} |\Delta x_k|$ and $\|\tilde{\mathbf{J}}\|_F$. One may consider using dimensionless parameters by normalizing each parameter by its nominal design value. This way, we can use our same procedure to construct an optimal set $\mathbf{A}'$ that minimizes the relative errors of the parameters instead of their absolute errors.

5. CONCLUSIONS

In summary, we have validated that our proposed general measurement configuration optimization method can assist in the accurate reconstruction of a complex deep-etched multilayer grating in the 65 nm node-patterned wafer. The simulation and experiment demonstrate the potential of the proposed method for being applied in the process control of advanced integrated circuit (IC) manufacturing. We conclude that the application of the proposed method is not limited in optical scatterometry: for example, it is also applicable for optimizing the measurement configuration in optical microscopy-based wafer inspection systems. We believe the present work will provide a different point of view for the accurate nanostructure reconstruction in IC manufacturing.

Funding. National Natural Science Foundation of China (NSFC) (51475191, 51405172, 51575214, 51525502); Natural Science Foundation of Hubei Province of China (2015CFB278, 2015CFA005); Program for Changjiang Scholars and Innovative Research Team in University of China (IRT13017); Gift Award from Cisco Systems Inc. (CG 587589).

Acknowledgment. The authors would like to thank Prof. Luke Olson for the useful discussions. We are also grateful to Cisco Systems Inc. for access to its Arcetri cluster. Portions of this work were presented at the SPIE Advanced Lithography conference [17] in February 2016.

REFERENCES

1. C. J. Raymond, M. R. Murnane, S. L. Prins, S. S. H. Naqvi, J. W. Hosch, and J. R. McNeil, "Multiparameter grating metrology using optical scatterometry," J. Vac. Sci. Technol. B **15**, 361–368 (1997).
2. X. Niu, N. Jakatdar, J. Bao, and C. J. Spanos, "Specular spectroscopic scatterometry," IEEE Trans. Semicond. Manuf. **14**, 97–111 (2001).
3. H. Huang and F. Terry, Jr., "Spectroscopic ellipsometry and reflectometry from gratings (scatterometry) for critical dimension measurement and in situ, real-time process monitoring," Thin Solid Film **455**, 828–836 (2004).
4. H. J. Patrick, T. A. Gemer, Y. F. Ding, H. W. Ro, L. J. Richter, and C. L. Soles, "Scatterometry for in situ measurement of pattern flow in nanoimprinted polymers," Appl. Phys. Lett. **93**, 233105 (2008).
5. Y. N. Kim, J. S. Paek, S. Rabello, S. Lee, J. T. Hu, Z. Liu, Y. D. Hao, and W. McGahan, "Device based in-chip critical dimension and overlay metrology," Opt. Express **17**, 21336–21343 (2009).
6. M. G. Faruk, S. Zangooie, M. Angyal, D. K. Watts, M. Sendelbach, L. Economikos, P. Herrera, and R. Wilkins, "Enabling scatterometry as an in-line measurement technique for 32 nm BEOL application," IEEE Trans. Semicond. Manuf. **24**, 499–512 (2011).
7. R. M. Al-Assaad and D. M. Byrne, "Error analysis in inverse scatterometry. I. Modeling," J. Opt. Soc. Am. A **24**, 326–338 (2007).
8. T. Novikova, A. De Martino, S. B. Hatit, and B. Drevillon, "Application of Mueller polarimetry in conical diffraction for critical dimension measurements in microelectronics," Appl. Opt. **45**, 3688–3697 (2006).
9. S. Liu, X. Chen, and C. Zhang, "Development of a broadband Mueller matrix ellipsometer as a powerful tool for nanostructure metrology," Thin Solid Film **584**, 176–185 (2015).
10. J. Zhu, S. Liu, X. Chen, C. Zhang, and H. Jiang, "Robust solution to the inverse problem in optical scatterometry," Opt. Express **22**, 22031–22042 (2014).
11. Y. Ku, S. Wang, D. Shyu, and N. Smith, "Scatterometry-based metrology with feature region signatures matching," Opt. Express **14**, 8482–8491 (2006).
12. P. Vagos, J. Hu, Z. Liu, and S. Rabello, "Uncertainty and sensitivity analysis and its applications in OCD measurement," Proc. SPIE **7272**, 72721N (2009).
13. H. Gross and A. Rathsfeld, "Sensitivity analysis for indirect measurement in scatterometry and the reconstruction of periodic grating structures," Wave Random Complex **18**, 129–149 (2008).
14. X. Chen, S. Liu, C. Zhang, and H. Jiang, "Measurement configuration optimization for accurate grating reconstruction by Mueller matrix polarimery," J. Micro/Nanolithogr. MEMS MOEMS **12**, 033013 (2013).
15. P. C. Logofatu, "Sensitivity analysis of grating parameter estimation," Appl. Opt. **41**, 7179–7186 (2003).
16. P. C. Logofatu, "Phase-modulation scatterometry," Appl. Opt. **41**, 7187–7192 (2002).
17. J. Zhu, Y. Shi, S. Liu, and L. L. Goddard, "Generalized measurement configuration optimization for accurate reconstruction of periodic nanostructures using optical scatterometry," Proc. SPIE **9778**, 977823 (2016).
18. T. A. Germer, H. J. Patrick, R. M. Silver, and B. Bunday, "Developing uncertainty analysis for optical scatterometry," Proc. SPIE **7272**, 72720T (2009).
19. Z. Dong, S. Liu, X. Chen, and C. Zhang, "Determination of an optimal measurement configuration in optical scatterometry using global sensitivity analysis," Thin Solid Films **562**, 16–23 (2014).
20. X. Chen, S. Liu, H. Gu, and C. Zhang, "Formulation of error propagation and estimation in grating reconstruction by a dual-rotating compensator Mueller matrix polarimeter," Thin Solid Films **571**, 653–659 (2014).
21. R. Zhou, C. Edwards, A. Arbabi, G. Popescu, and L. L. Goddard, "Detecting 20 nm wide defects in large area nanopatterns using optical interferometric microscopy," Nano Lett. **13**, 3716–3721 (2013).

22. R. Zhou, C. Edwards, G. Popescu, and L. L. Goddard, "9 nm node wafer defect inspection using visible light," Proc. SPIE **9050**, 905017 (2014).
23. R. Zhou, C. Edwards, C. Bryniarski, G. Popescu, and L. L. Goddard, "9 nm node wafer defect inspection using three-dimensional scanning: a 405 nm diode laser, and a broadband source," Proc. SPIE **9424**, 942416 (2015).
24. B. M. Barnes, M. Y. Sohn, F. Goasmat, H. Zhou, and R. M. Silver, "Scatterfield microscopy of 22 nm node patterned defects using visible and DUV light," Proc. SPIE **8324**, 83240F (2012).
25. B. M. Barnes, F. Goasmat, M. Y. Sohn, H. Zhou, and R. M. Silver, "Enhancing 9 nm node dense patterned defect optical inspection using polarization, angle, and focus," Proc. SPIE **8681**, 86810E (2013).
26. B. M. Barnes, M. Y. Sohn, F. Goasmat, H. Zhou, A. E. Vladar, R. M. Silver, and A. Arceo, "Three-dimensional deep sub-wavelength defect detection using $\lambda = 193$ nm optical microscopy," Opt. Express **21**, 26219–26226 (2013).
27. M. A. Henn, H. Gross, F. Scholze, M. Wurm, C. Elster, and M. Bar, "A maximum likelihood approach to the inverse problem of scatterometry," Opt. Express **20**, 12771–12786 (2012).
28. M. G. Moharam, E. B. Grann, D. A. Pommet, and T. K. Gaylord, "Formulation for stable and efficient implementation of the rigorous coupled-wave analysis of binary gratings," J. Opt. Soc. Am. A **12**, 1068–1076 (1995).
29. L. Li, "Use of Fourier series in the analysis of discontinuous periodic structures," J. Opt. Soc. Am. A **13**, 1870–1876 (1996).
30. S. Liu, Y. Ma, X. Chen, and C. Zhang, "Estimation of the convergence order of rigorous coupled-wave analysis for binary gratings in optical critical dimension metrology," Opt. Eng. **51**, 081504 (2012).
31. J. Zhu, S. Liu, H. Jiang, C. Zhang, and X. Chen, "Improved deep-etched multilayer grating reconstruction by considering etching anisotropy and abnormal errors in optical scatterometry," Opt. Lett. **40**, 471–474 (2015).
32. M. Sendelbach and C. Archie, "Scatterometry measurement precision and accuracy below 70 nm," Proc. SPIE **5038**, 224–238 (2003).
33. F. Argenti, G. Torricelli, and L. Alparone, "MMSE filtering of generalised signal-dependent noise in spatial and shift-invariant wavelet domains," Signal Process. **86**, 2056–2066 (2006).
34. N. Acito, M. Diani, and G. Corsini, "Signal-dependent noise modeling and model parameter estimation in hyperspectral images," IEEE Trans. Geosci. Remote Sens. **49**, 2957–2971 (2011).
35. A. Kato and F. Scholze, "Effect of line roughness on the diffraction intensities in angular resolved scatterometry," Appl. Opt. **49**, 6102–6110 (2010).
36. X. Chen, Y. Shi, H. Jiang, C. Zhang, and S. Liu, "Nondestructive analysis of lithographic patterns with natural line edge roughness from Mueller matrix ellipsometric data," Appl. Surf. Sci. (to be published).